Radio emission from merging galaxy clusters : characterizing shocks, magnetic fields and particle acceleration

Weeren, R.J. van

CHAPTER 12

LOFAR Abell 2256 observations between 18 and 67 MHz

Abstract.

Abell 2256 is one of the best known examples of a galaxy cluster hosting large-scale diffuse radio emission that is unrelated to individual galaxies. It contains both a giant radio halo and a relic as well as number of head-tail sources and smaller diffuse steep-spectrum radio sources. The origin of radio halos and relics is still being debated, but over the last years it has become clear that the presence of these radio sources is closely related to galaxy cluster merger events. Here we present the first LOFAR Low-band antenna (LBA) observations of Abell 2256 between 18 and 67 MHz. To our knowledge, the images made at 20, 30 and 63 MHz are the deepest ever obtained at frequencies below 100 MHz. Both the radio halo and the giant relic are clearly detected in the LBA image at 63 MHz, and the diffuse radio emission remains visible at frequencies as low as 20 MHz. The observations confirm the presence of a previously claimed ultra-steep spectrum source to the west of the cluster center with a spectral index of -2.3 ± 0.4 between 63 and 153 MHz. The steep spectrum suggests that this source is an old part of the head-tail radio source C in the cluster. For the radio relic we find an integrated spectral index of -0.81 ± 0.03, after removing the flux contribution from the other sources. This flat integrated spectral index could indicate that in the observed frequency range the electron cooling time is longer than the age of the relic. If shocks are assumed to be responsible for relic formation, this would imply that the relic traces a shock that only recently formed (within the last ~ 0.1 Gyr). In the radio halo region we find indications of low-frequency spectral steepening.

R. J. van Weeren et al., on behalf of the LOFAR collaboration

to be submitted

12.1 Introduction

Radio halos and relics are diffuse radio sources, unrelated to individual galaxies, found in disturbed galaxy clusters (see the reviews by Feretti 2005; Ferrari et al. 2008, and references therein). These sources are rare – only several dozen examples have been previously identified. The presence of diffuse radio emission indicates magnetic fields and relativistic particles in the intracluster medium (ICM) that are (re)accelerated in-situ, due to the limited lifetime of the synchrotron emitting electrons (Jaffe 1977). The origin of this diffuse emission is presently still being debated and is crucial for understanding the non-thermal component in the ICM and particle acceleration mechanisms.

Over the last decade it has become clear that the diffuse radio emission in galaxy clusters is often related to galaxy cluster merger events (e.g., Cassano et al. 2010b; van Weeren et al. 2010). It is also predicted in the framework of the concordant cosmological model that galaxy clusters grow as a result of the mergers of smaller clusters and sub-structures creating turbulence and shocks (e.g., Markevitch et al. 2002; Vazza et al. 2006; Russell et al. 2010) in their ICM.

Diffuse sources in merging clusters have commonly been classified as radio *relics* and *halos*. In this context, elongated filamentary sources have generally been called relics. Relics are usually further subdivided into three classes (see also Kempner et al. 2004). (1) *Radio Gischt* are large extended arc-like sources mostly found in the outskirts of galaxy clusters. They are often highly polarized at frequencies $\gtrsim 1$ GHz (20% or more). It has been proposed that they directly trace shock waves (Ensslin et al. 1998; Miniati et al. 2001), in which particles are accelerated by the diffusive shock acceleration mechanism (DSA; Blandford & Ostriker 1978; Drury 1983; Blandford & Eichler 1987; Jones & Ellison 1991; Malkov & O'C Drury 2001) in a first-order Fermi process. A related scenario is that of shock re-acceleration of pre-accelerated electrons in the ICM, which may be a more efficient mechanism in weak shocks (e.g., Markevitch et al. 2005; Giacintucci et al. 2008; Kang & Ryu 2011) and might be needed because the efficiency with which collisionless shocks can accelerate particles is unknown, and might not be enough (e.g., Macario et al. 2011) to produce the observed radio brightness. The pre-accelerated electrons could for example originate from the radio galaxies in clusters. (2) *Radio phoenices* are most likely related to fossil radio plasma from previous episodes of AGN activity adiabatically compressed by merger shock waves, boosting the radio emission (Enßlin & Gopal-Krishna 2001; Enßlin & Brüggen 2002). (3) *AGN relics* trace old (uncompressed) radio plasma from previous episodes of AGN activity. The radio spectra of both radio phoenices and AGN relics are expected to be steep ($\alpha \lesssim -1.5$, $F_\nu \propto \nu^\alpha$, where α is the spectral index) and curved due to synchrotron and Inverse Compton (IC) losses.

Radio halos are extended sources with sizes of about a Mpc. They are typically unpolarized and their radio emission roughly follows the thermal X-ray emission from the ICM. Two classes of models have been put forward to explain the origin of these halos. In the first model the energetic electrons are the secondary products of proton-proton collisions (e.g., Dennison 1980; Blasi & Colafrancesco 1999; Dolag & Enßlin 2000; Enßlin et al. 2011). In the second model the electrons are re-accelerated in-situ through a second order Fermi mechanism by magneto-hydrodynamical (MHD) turbulence (e.g., Brunetti et al. 2001; Petrosian 2001) The existence of ultra-steep spectrum radio halos (USSRH, $\alpha \lesssim -1.5$, Brunetti et al. 2008; Macario et al. 2010; Dallacasa et al. 2009) does not support a secondary origin for the electrons as it requires an unrealistic amount of energy in the relativistic protons (Brunetti 2004).

Abell 2256 is a nearby, $z = 0.0581$ (Struble & Rood 1999), cluster that contains a giant

radio halo, relic and a large number of tailed radio galaxies. The relic has a large integrated flux, compared to other relics, of about 0.5 Jy at 1.4 GHz. The large angular extent of the diffuse emission and its large integrated flux make it a prime target for low-frequency observations which typically suffer from low spatial resolution and sensitivity, compared to observations at high frequencies ($\gtrsim$ 1 GHz).

The cluster hosts a handful of head-tail radio sources as well as several smaller diffuse radio sources not directly related to individual galaxies (Bridle & Fomalont 1976; Bridle et al. 1979; Röttgering et al. 1994; Miller et al. 2003; Clarke & Ensslin 2006; Brentjens 2008; Intema 2009; van Weeren et al. 2009a; Kale & Dwarakanath 2010). X-ray and optical observations provide strong evidence that A2256 is undergoing a merger event between a main cluster ($T_{\rm ICM} \sim$ 7–8 keV), a major sub-structure ($T_{\rm ICM} \sim$ 4.5 keV) and, possibly, a third infalling group (Briel et al. 1991; Briel & Henry 1994; Sun et al. 2002; Berrington et al. 2002; Miller et al. 2003). The cluster has an X-ray luminosity of $L_{\rm X,\ 0.1-2.4\ keV} = 3.7 \times 10^{44}$ erg s^{-1} (Ebeling et al. 1998).

At wavelengths larger than 1 m, the diffuse radio emission in A2256 has been studied with the GMRT at 150 MHz (Intema 2009; Kale & Dwarakanath 2010), and with the WSRT between 115 and 165 MHz (van Weeren et al. 2009a; Intema 2009). The VLSS 74 MHz image (Cohen et al. 2007) shows a hint of diffuse emission, and the 8C and 6C survey images (Hales et al. 1995; Masson & Mayer 1978) have too low resolution to properly separate the flux contributions from the discrete sources. The observations by Intema (2009) and van Weeren et al. (2009a) showed the presence of three previously unknown diffuse sources with steep radio spectra ($\alpha \lesssim -1.5$). These steep radio spectra suggest that these sources trace old radio plasma from previous episodes of AGN activity in the cluster.

In this paper we present the first LOFAR observations of Abell 2256, focussing on the frequency range around 63 MHz. The layout of this paper is as follows: In Sect. 12.2 we give an overview of the observations and the data reduction. In Sect. 12.2.1 we present the results, including the radio images and a spectral index map. We conclude with a discussion and the results presented in Sects. 2.6 and 2.7, respectively. Throughout this paper we assume a ΛCDM cosmology with $H_0 = 71$ km s^{-1} Mpc^{-1}, $\Omega_{\rm m} = 0.3$, and $\Omega_\Lambda = 0.7$.

12.2 Observations & data reduction

Abell 2256 was observed with LOFAR on July 15, 2011, with the LBA system for 10 hrs, mostly during night-time. Complete frequency coverage between 18 and 67 MHz was obtained, although there were a few gaps at frequencies where usually strong radio frequency interference (RFI) is present. All four linear correlation products were recorded. The observed frequency range was divided into 244 sub-bands (IFs), each having a bandwidth of 0.1953 MHz. Each sub-band was subdivided into 64 frequency channels. The integration time was 1 s. The so-called LBA_OUTER configuration was used for the LBA stations. In this mode 48 (of 96) LBA antennas are used, located mostly in the outer part of the antenna fields/stations (which have diameters of about 80 m). This increases the sidelobe levels for the station beams but reduces the field of view (FOV) with respect to other station antenna configurations.

In total 25 stations (8 remote and 17 core) were used for the A2256 observation. The longest baseline, between stations RS208 and RS509, is about 80 km and the shortest baselines corresponds to $\sim$ 90 m. The uv-coverage is shown in Fig. 12.1. The FOV (FWHM of the primary beam) is about 4.6° and 9.2° at 60 and 30 MHz, respectively. It should be noted though that

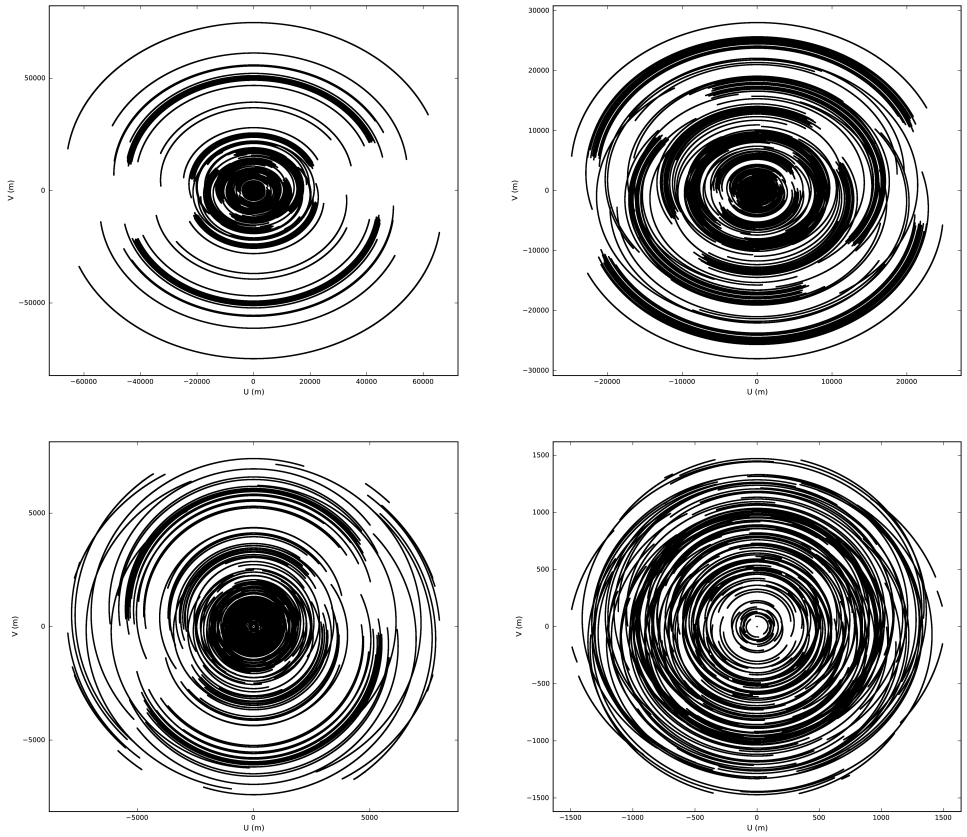

Figure 12.1: UV-coverage of the observations. The outer UV-coverage is shown in the top left frame, the next frames progressively zoom inwards. The relatively broad bandwidth fills the uv-plane radially (not shown in the figures).

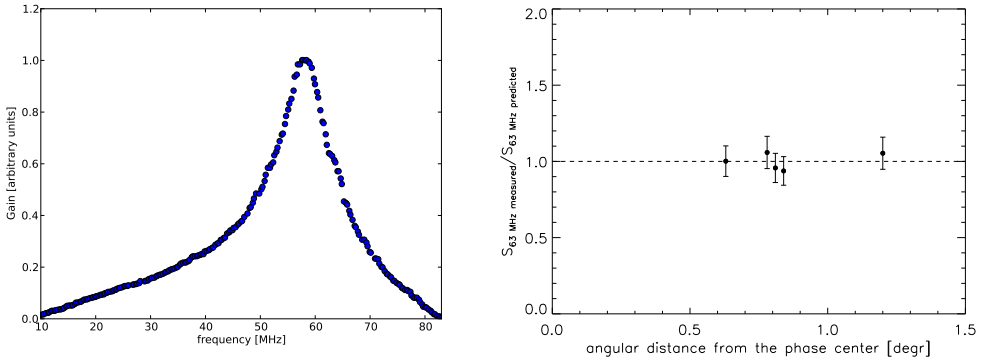

Figure 12.2: Left: LBA global bandpass. The bandpass peaks at about 58 MHz. Right: Measured LOFAR fluxes and predicted fluxes for 5 bright sources in the A2256 field. For all these sources 8C, VLSS, 7C, WENSS, and NVSS fluxes were available. We used second order polynomial fits in $\log(S) - \log(\nu)$ space to compute the predicted 63 MHz fluxes. An overall scaling factor of 1.23 was applied to the LOFAR fluxes. The error bars display the adopted 10% uncertainty in the flux scale.

the stations beams are complex-valued, time and direction dependent, and slightly differ from station to station.

As a first step, the RFI was flagged with the AOFlagger (Offringa et al. 2010) using default settings, and the first and last two channels at the edge of each sub-band were removed. The amount of RFI flagged was typically only few percent or less above 30 MHz. The amount of RFI increases strongly below $\sim$ 28 MHz. Between 30% and 70% had to be flagged below this frequency for most sub-bands, with at least some of this attributable to short-wave radio transmissions. The RFI situation was somewhat better after midnight. After flagging, the data were averaged in time to 5 s.

For this A2256 observation, the bright radio sources Cas A, Cyg A and Vir A (the so-called "A-team sources") were located 34, 42, and 74° away from the phase center, respectively. These sources have integrated flux densities of about 17764, 17205, and 2085 Jy at 74 MHz, respectively. Therefore the attenuated signals from Cas A and Cyg A are still much stronger (more than a factor of 10) than the signal from the sources in the primary FOV. Their amplitudes are strongly modulated as they move in and out of the station beam sidelobes. For the first 2.5 hr of the observations Vir A also affects the observed visibilities, until the source sets below the horizon. At frequencies $\lesssim$ 35 MHz, 3C 390.3 (located 4.7° from the phase center) is sufficiently bright, 145 ± 14 Jy at 38 MHz (Hales et al. 1995), that it needs to be treated separately as described below.

The first calibration step consisted of the removal of the three "A-team" sources. Below 35 MHz, 3C 390.3 was also included in the calibration model. For the models of the A-team sources and 3C 390.3 we used the clean component models at 74 MHz from VLA A-array[1] observations (Kassim et al. 2007) with resolution of 25″. For all calibration steps we used the BlackBoard Selfcal (BBS) software (e.g., Heald et al. 2010). Full polarization direction

[1] http://lwa.nrl.navy.mil/tutorial/

dependent complex gain solutions were obtained for the three A-team sources (and 3C 390.3 below 35 MHz) independently per sub-band. Vir A was only included in the calibration model for the first 2.5 hr. In general, high-quality solutions were obtained for Cas A and Cyg A, while the solutions for Vir A and 3C 390.3 were noisier due to their lower apparent fluxes. The A-team sources were then subtracted ("peeled") with the estimated gain solutions. 3C390.3 was not subtracted as it is in the main FOV below 35 MHz and used in subsequent calibration steps. After removal of the A-team sources from the visibility data we performed another round of flagging with the AOFlagger and averaged the data to 4 channels and 10 sec per sub-band, to decrease the size of the dataset whilst mitigating bandwidth and time smearing effects in the central FOV.

The responses of the LBA antennas depends on the observed frequency (see Fig. 12.2). The LBA response was obtained from observations of Cyg A. Observations carried out over the course of several months show that the bandpass response is stable at the few precent level or better. We divided out this sensitivity pattern to avoid the need to obtain amplitude calibration solutions for each individual sub-band. The reason behind this is that the signal to noise ratio (SNR) per sub-band is not sufficient to obtain good gain solutions due to the limited effective bandwidth of 0.183 MHz. By combining several sub-bands this limitation can be overcome. However, a problem at low frequencies is that the ionospheric phase distortions are frequency dependent, and this effect increases towards lower frequencies. At about 60 MHz this means that if this effect is not included only about 1 MHz bandwidth can be used for calibration, depending on the ionospheric conditions (e.g., eq. 4 from Intema et al. 2009). To obtain high-quality solutions more bandwidth is required. This can be accomplished by solving for the differential total electron content: TEC. This adds a frequency dependent phase term (TEC/ν). During the calibration we therefore solve for a single polarization dependent complex gain factor (to set the amplitudes and capture other instrumental effects such as clock drift) and polarization independent TEC value per station and time-slot (10 s). We used 20 sub-bands around 20 MHz, 20 around 30 MHz, and 30 around 63 MHz for this "global calibration" including TEC solving. Due to computational limitations we concentrated our efforts on these three frequency ranges.

We calibrated the data against a 74 MHz 80″ VLSS model of the field around A2256 (covering $15^\circ \times 15^\circ$), assuming that all sources are unpolarized, which is a reasonable assumption at these low frequencies. We used an overall flux scaling with a spectral index of -0.8 to get a first order approximation of the flux-scale. For computing the model visibilities we included the complex beam attenuation of each station beam.

12.2.1 Primary beam correction, absolute flux-scale and self-calibration

We applied the calibration solutions and corrected the data for the each station's beam response in the phase center. Note that it is only possible to correct for the stations beam response in a single direction. For the other directions (within the main FOV) this correction is only a first order approximation. The entire FOV (to an attenuation factor of 0.15 compared to the beam center) was then imaged and cleaned with Casapy with w-projection (Cornwell et al. 2005, 2008), 768 w-planes in total. Ideally, to create flux corrected wide-field images, the time-variable direction dependent effects need to be taken into account (e.g., Bhatnagar et al. 2008). This functionality is still under development. We made images with "briggs" weighting (Briggs 1995) with robust=-0.1, a compromise between resolution and sensitivity to emission at larger spatial scales. We combined groups of sub-bands around 63, 30 and 20 MHz for multi-frequency

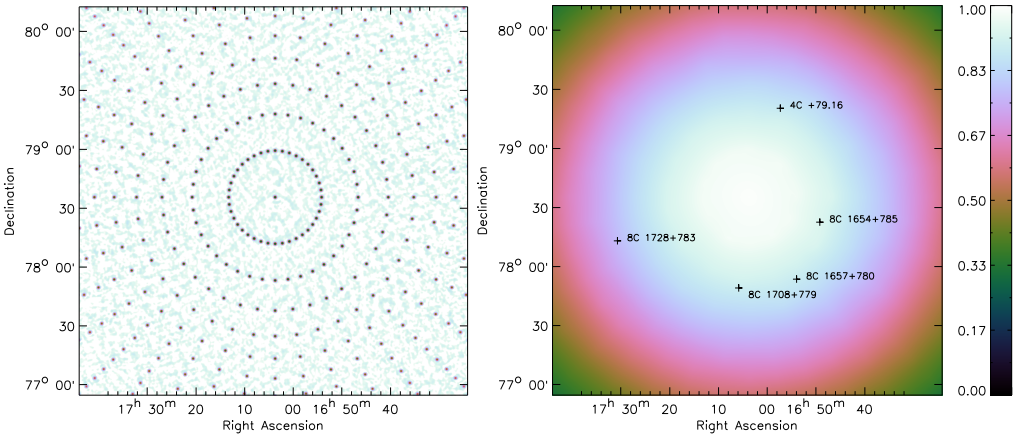

Figure 12.3: Left: Simulated point sources of 1 Jy in the A2256 field at 63 MHz. Right: Effective primary beam attenuation of the A2256 observations at 63 MHz, fitting a surface to the integrated fluxes of the sources in the left panel. Sources which were used to obtain the flux-scale are marked.

synthesis imaging, producing three broadband images.

To obtain the correct relative flux scale over the field we simulated a dense grid of 1 Jy point sources in the A2256 field including the LOFAR station beam. This grid is illustrated in Fig. 12.3. With this we could track the effective beam attenuation as a function of position in the FOV. This simulated dataset (with the same frequency setup and uv-coverage as the observed data) was then imaged the same way as the observed A2256 data. We extracted the integrated fluxes for these simulated point sources using the `PyBDSM` source detection software[2]. A 2D surface was fitted to these extracted source fluxes using the `griddata` module from the python matplotlib, which employs a Delaunay triangulation[3]. This triangulated surface gives the effective sensitivity as function of position in the A2256 field and can be used to create a primary beam corrected image. We used the flux-corrected image to obtain an updated sky model (again with `PyBDSM`) for a subsequent round of self-calibration (the calibration strategy remaining unchanged).

The final images (robust=−0.1) have noise levels of 10, 43, 250 mJy beam^{-1} at 60, 30 and 20 MHz respectively. A lower resolution, robust=0.5 weighting, image at 63 MHz has a noise of 25 mJy beam^{-1}. See Table 12.1 for a summary of the resolution, bandwidth and sensitivity of the images. Thermal noise is expected to be around 2.5 mJy beam^{-1} at 63 MHz and 8 mJy beam^{-1} at 30 MHz.

The presence of residual ionospheric phase errors after calibration lead to a wider point source width. We measure a point source width that is about 20″ larger than the synthesized beamwidth at 63 MHz. This effect has also been seen for 74 MHz VLA observations (e.g., Cohen et al. 2007). At lower frequencies this worsens to 70″ and 180″ at 30 and 20 MHz, respectively. In this case the unresolved sources are elongated, distorted, and partly broken up into smaller components. Because of this reason, we only use the 63 MHz maps for quantitative

[2]see the LOFAR Imaging Cookbook at http://www.astron.nl/radio-observatory/lofar/lofar-imaging-cookbook
[3]http://matplotlib.sourceforge.net

Table 12.1: LOFAR LBA images

central frequency MHz	image bandwidth MHz	$\sigma_{\rm rms}$ mJy beam^{-1}	synthesized beam arcsec
63 (robust -0.1)	5.5	10	22×26
63 (robust 0.5)	5.5	25	52×62
30 (robust -0.1)	3.7	43	58×69
20 (robust -0.1)	3.7	250	108×116

analysis in this paper, while the 30 and 20 MHz maps are used for qualitative analysis until a more complete ionospheric correction is made.

To obtain and check the overall flux scale we measured the integrated fluxes for five bright sources in the FOV: 4C +79.16 , 8C 1654+785, 8C 1657+780, 8C 1708+779, and 8C 1728+783 (see Fig. 12.3). For these sources we collected flux measurements from the 1.4 GHz NVSS (Condon et al. 1998), 325 MHz WENSS (Rengelink et al. 1997), 151 MHz 7C (Hales et al. 2007), 74 MHz VLSS (Cohen et al. 2007) and 38 MHz 8C (Hales et al. 1995) surveys. We fitted second order polynomials to these flux measurements in $\log(S) - \log(\nu)$ space and compared the LOFAR flux measurements at 63 MHz against the predicted fluxes from the polynomial fits. The median of correction factors was used to tie the LOFAR images to an absolute flux-scale. The correction factor we found was modest, being 1.23 at 63 MHz. The spread in the individual correction factors is about 7%, see Fig 12.2 (right panel).

From this we adopt a conservative error in the LOFAR flux scale of 10% compared to these surveys.

12.2.2 Radio images

The 63 MHz images are displayed in Fig. 12.4 and the 20 and 30 MHz images in Fig. 12.5. We labelled some of the known sources in the cluster following the scheme from Bridle & Fomalont (1976); Röttgering et al. (1994); van Weeren et al. (2009a). The LOFAR 63 MHz image reveals some of the well-known tailed radio sources (A, B, F), the main relic (G and H), and part of the radio halo. A hint of the long and straight head-tail source C is also visible.

The main radio relic and halo are somewhat better visible in the lower resolution 63 MHz image (Fig. 12.4, right panel). Interestingly, the LOFAR image also reveals source AG+AH. This source has only been recently discovered (van Weeren et al. 2009a) and is not visible in the deep VLA L-band observations from the VLA (Clarke & Ensslin 2006), implying a steep spectral index. We do not detect the steep spectrum source AI, but this was expected since the integrated flux of this source is about a factor of two lower than AG+AH at 325 MHz. The 30 MHz image reveals source F and the combined emission from A and B. The relic is also detected. At 20 MHz the ionospheric phase distortions are quite severe, causing the relic to partly blend with sources F and the A+B complex.

An overlay of the 63 MHz image with a VLA L-band image is shown in Fig. 12.6 (right panel). For this we combined 1369, 1413, 1513, and 1703 MHz VLA C-array images from Clarke & Ensslin (2006). These images were convolved to a common resolution of $16'' \times 16''$ and combined adopting a flux scaling according to a spectral index, $\alpha = -1$. It is interesting

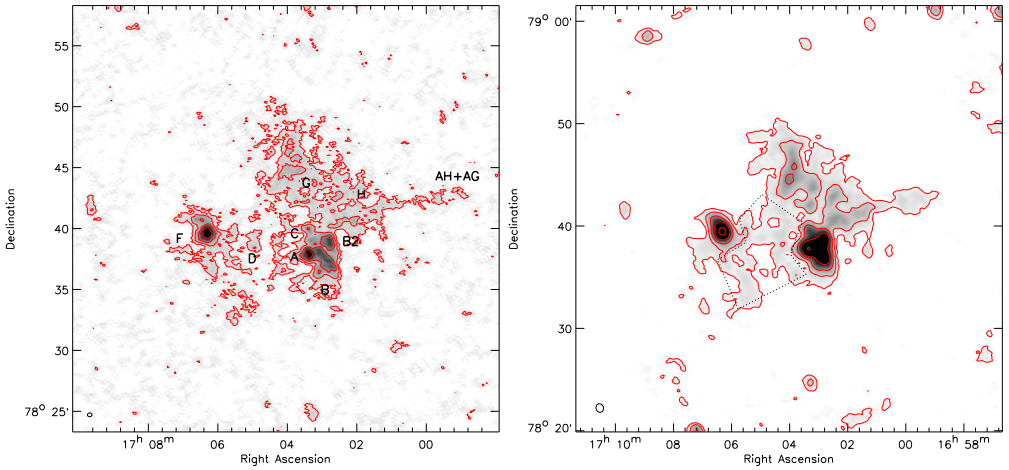

Figure 12.4: A2256 61-67 MHz images. Left: High-resolution, $22'' \times 26''$, image made with robust=-0.1 weighting. Contour levels are drawn at $[1, 2, 4, \ldots] \times 3\ \sigma_{\rm rms}$. Right: Low-resolution image, $52'' \times 62''$, image made with robust=0.5 weighting. The area for the halo spectral index measurement is indicated by the dotted lines. Contours are drawn as in the left panel.

to note the differences between the L-band and LBA images around the A+B complex. The VLA image peaks in brightness at the "heads" of the head-tail sources, while the LOFAR image mainly shows the "tails". The steep spectrum B2 region, noticed by Intema (2009), also clearly stands out. A Chandra X-ray overlay is shown in Fig. 12.7.

12.2.3 Spectral index map and integrated fluxes

We made a spectral index map between 63 and 351 MHz, making use of the WSRT 351 MHz map from Brentjens (2008). We made a LOFAR image with uniform weighting of the visibilities and applying a Gaussian taper in the uv-plane to approximately match up the WSRT resolution of $67'' \times 67''$. To increase the SNR per beam for the diffuse emission we convolved both images to $100''$ resolution, pixels below $3\sigma_{\rm rms}$ were blanked. The LOFAR-WSRT spectral index map is shown in Fig. 12.6 (left panel).

The spectral index map reveals that the relic has a relatively flat spectral index of about -0.8 with variations of 0.3 in α across the structure. For the parts of the radio halo where the spectral index can be measured we find α to be in the range -1.0 to -1.7. For source F the spectral index is around -1.0. For the combined emission from AH and AG we find a steep spectral index between -2.2 to -1.7.

We extracted the integrated fluxes for sources in the cluster from the 63 MHz image, see Table 12.2. The integrated fluxes of the radio halo and relic (source G+H) are difficult to measure as they are partly blended with some of the complex head-tail radio sources in the cluster. To estimate their flux contribution we used both the high and low resolution images (Fig. 12.4). From the high resolution image we measured the fluxes for source F, and the combined emission from A and B (A+B). Head-tail source C contributes a significant amount of flux to the relic

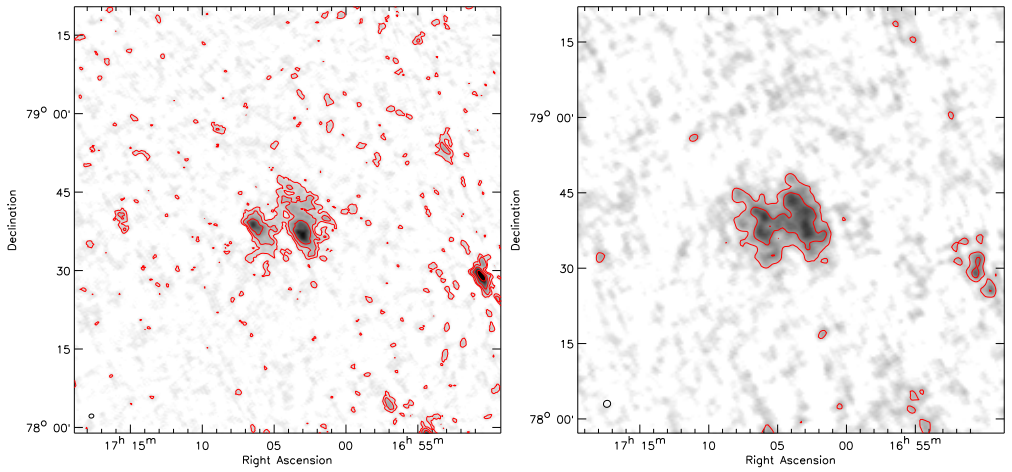

Figure 12.5: A2256 30 and 20 MHz images. Left: 28–32 MHz image with a resolution, 58″×69″. Contour levels are drawn at $[1, 2, 4, \ldots] \times 3\ \sigma_{\rm rms}$. Right: 18–22 MHz image with a resolution of 108″ × 116″. Contours are drawn as in the left panel. Both images were made with robust=0.1 weighting. The bright compact source to the west around RA 17^h51^m is 8C 1654+785.

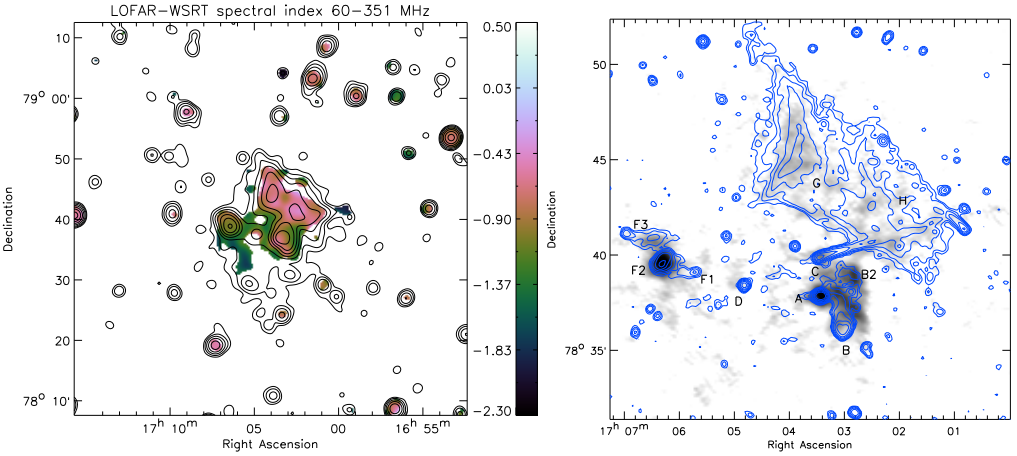

Figure 12.6: Left: LOFAR LBA - WSRT spectral index map between 63 and 351 MHz. Total intensity contours at 351 MHz are shown at levels of $[1, 2, 4, 8, \ldots] \times 1.0$ mJy beam^{-1}. The 351 MHz image comes from Brentjens (2008). Right: LOFAR LBA 63 MHz image overlaid with VLA L-band C-array contours. The contour levels are drawn at $[1, 2, 4, 8, \ldots] \times 90\ \mu$Jy beam^{-1}.

Table 12.2: 63 MHz source fluxes

Source	$S_{63\mathrm{MHz}}$ Jy	α_{63}^{153}
A+B	5.1 ± 0.6	-1.1 ± 0.2
F	2.8 ± 0.3	-1.2 ± 0.2
AG + AH	0.75 ± 0.10	-2.3 ± 0.4
relic (G + H)	5.6 ± 0.8	-0.81 ± 0.03^a
halo	6.6 ± 1.3	-1.3 ± 0.1^b

[a] from a polynomial fit in $\log(S) - \log(\nu)$ space, see Fig. 12.8 (left panel)
[b] between 63 and 351 MHz, α taken from Fig. 12.8 (right panel)

emission, as judged from the GMRT 153 MHz image from Intema (2009). In the 63 MHz image the source blends with the radio relic, making it impossible to obtain a reliable flux estimate. Using the 153 MHz GMRT image (giving a flux of 0.48 ± 0.05 Jy) and the reported 327 MHz VLA flux (0.247 ± 0.020 Jy, Röttgering et al. 1994) we find $\alpha = -0.87 \pm 0.17$ for source C. Extrapolating this to 63 MHz, we estimate a flux of 1.05 Jy. To measure the relic flux we summed the flux over the same region as indicated in fig. 10 by Brentjens (2008). After subtracting the flux contribution for source C we obtain a relic flux of 5.6 Jy, with an estimated uncertainty of 15%. A power-law fit through the relic flux measurements at 1369 (Clarke & Ensslin 2006), 351 (Brentjens 2008), 153 (Intema 2009), and 63 MHz gives a spectral index of -0.81 ± 0.03, see Fig. 12.8. For the radio halo we find a flux of 6.6 ± 1.3 Jy from Fig. 12.4 (right panel), integrating over the entire halo area as defined by the 351 MHz image.

12.3 Discussion

The results on the radio spectra for source F, AG+AH, and the radio halo and relic are discussed in the following subsections.

12.3.1 Source F

Source F is known for its complex Z-shape morphology (see Fig. 12.6) and steep radio spectrum (e.g., Bridle et al. 1979). The source is composed out of three smaller structures: F1, F2 and F3. The brightest component F2 has a toroidal filamentary shape (Röttgering et al. 1994; Miller et al. 2003; Intema 2009). F3 has been classified as a head-tail radio source associated with galaxy 122 (Fabricant et al. 1989). No optical counterparts have been found for F1 and F2, and their origin is still being debated. Bridle et al. (1979) suggested that all three components are the tail of galaxy 122, this scenario is also discussed by Brentjens (2008). In another scenario F2 could be the compressed fossil radio plasma from previous episodes of AGN activity (Enßlin & Gopal-Krishna 2001; Enßlin & Brüggen 2002), in this case the fossil plasma could also have originated from galaxy 122. This agrees with the observed toroidal shape (Enßlin & Brüggen 2002).

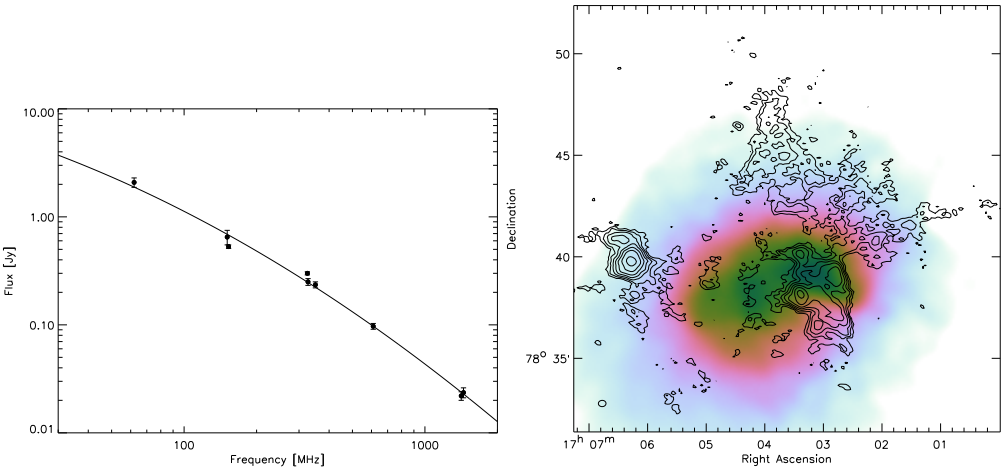

Figure 12.7: Left: Radio spectrum of F2. The fluxes were taken from the Brentjens (2008). Solid line is a second order polynomial fit through the flux measurements in $\log(S) - \log(\nu)$ space. During the fitting procedure we assumed 10% uncertainty in the flux measurements because flux measurement are not all consistent within their 1σ reported error. This prevents the fit to be forced to go through a few measurements with small reported uncertainties. Right: Chandra 0.5–7 keV ACIS-I/S co-added image smoothed by a variable-width Gaussian, fig. 1 from Sun et al. (2002). LOFAR 63 MHz contours from the high-resolution image are overlaid at levels of $[1, 2, 4, 8, \ldots] \times 3.5\ \sigma_{\rm rms}$.

We collected flux measurements for F2 from the literature (see Brentjens 2008), these are plotted in Fig. 12.7. The spectrum for F2 is clearly curved with the spectral index flattening towards lower frequencies. From the fit, see caption Fig. 12.7, we find a spectral index of -0.95 between 63 and 153 MHz. Between 150 and 350 MHz Kale & Dwarakanath (2010) reported $\alpha = -1.10 \pm 0.05$ (but no flux measurements were reported for F2). We however find a spectral index of -1.34 between 150 and 350 MHz using the polynomial fit. The reason for the difference is unclear, but it should be noted that the measurements from the literature are not consistent within their reported uncertainties. Between 610 and 1400 MHz we obtain $\alpha = -1.67$, much steeper than at low-frequencies. Brentjens (2008) estimated a possible break frequency to be located at 26 MHz, assuming a constant magnetic field of 7.3 μG and an ageing time of 0.2 Gyr. The 63 MHz flux measurement indicates the spectrum continues to flatten. However, high-resolution measurements below 60 MHz are needed to determine the possible underlying ("zero ageing") power-law component. The origin of source F2 remains unclear, although it is likely the source is somehow related to the fossil radio plasma from previous phases of AGN activity given its brightness and steep radio spectrum.

12.3.2 Source AG+AH

The combined emission from source AG+AH is detected in the LOFAR 63 MHz image. With the non-detection of these sources in the deep L-band image from Clarke & Ensslin (2006), van Weeren et al. (2009a) determined that $\alpha < -1.95$ between 325 and 1369 MHz. Between 140 and

351 MHz, using WSRT observations, the spectral index is -2.05 ± 0.14 at a resolution of 175″ (at this resolution the flux of this feature partly blends with the relic emission). With the 153 MHz image from Intema (2009) we find a flux of 95 ± 10 mJy for the combined emission from AG+AH. From the GMRT 325 MHz image we reported a flux of 19 ± 2 mJy (van Weeren et al. 2009a). This gives a spectral index of -2.1 ± 0.2 between these two frequencies, in agreement with the earlier reported result of -2.05 ± 0.14. The LOFAR flux is 0.75 ± 0.10 Jy for this source. This results in a spectral index of -2.3 ± 0.4 between 63 and 153 MHz. At low-frequencies the spectrum thus remains steep, although the uncertainty in the spectral index is too large to rule out a spectral turnover.

We consider the possibility that this emission is related to the head-tail source C. Following Miley (1980); Brentjens (2008) for a constant magnetic field and no adiabatic losses the radiative lifetime/spectral age (τ) is given as

$$\tau = \frac{2.6\times10^{10}\sqrt{B}}{\left(B^2 + B^2_{\rm CMB}\right)(1+z)\nu_{\rm brk}}\ [\rm yr]\,, \tag{12.1}$$

where B is the magnetic field strength in μG, $B_{\rm CMB}\,[\mu{\rm G}] = 3.25(1+{\rm z})^2$ the equivalent magnetic field strength of the microwave background and $\nu_{\rm brk}$ the break frequency in MHz. The LOFAR 63 MHz flux measurement indicates that $\nu_{\rm brk}$ is located $\lesssim 50$ MHz as the spectrum is still very steep between 63 and 153 MHz. The magnetic field is difficult to estimate as the spectral shape is poorly constrained. With a reasonable value of 10 μG we obtain a spectral age of 0.1 Gyr. This increases to 0.2 Gyr for $B = 5\,\mu$G. In all cases we assumed $\nu_{\rm brk} = 50$ MHz. Röttgering et al. (1994) estimated a velocity (v) of ~ 2000 km s^{-1} for the head-tail source. Then the separation between the "head" and AG+AH would be $v \times \tau = 200$ kpc, for $B = 10\ \mu$G. AG+AH is located about 800 kpc (projected distance) from the head of C. A lower magnetic field strength of $B = 3.0\ \mu$G would give a distance of 600 kpc. It is also possible that the break frequency is located at a lower frequency. If the radio plasma from the tail (the AG+AH part) is compressed by the merger shock wave, the radiative age of the source could be older (about 0.5 Gyr or more, e.g., Dwarakanath & Kale 2009; Kale & Dwarakanath 2011). This makes it easier to explain the distance of (at least) 800 kpc. Given all the uncertainties, source AG+AH could indeed be an old part of the tail of source C.

12.3.3 Radio relic and halo

Giant radio relics are proposed to trace particles (re)accelerated at shocks via the DSA mechanism. In the linear test particle regime, the injection spectral index is related to the Mach number ($\mathcal{M}$) of the shock (e.g., Blandford & Eichler 1987)

$$\alpha_{\rm inj} = \frac{1}{2} - \frac{\mathcal{M}^2+1}{\mathcal{M}^2-1}\,. \tag{12.2}$$

If the properties of the shock remain unchanged and the age of the shock is larger than the electron cooling time, the integrated radio spectrum will be a power-law, with a spectral index about 0.5 units steeper than $\alpha_{\rm inj}$ (Miniati 2002). The radio spectrum of the relic has a power-law shape over the observed frequency range, with a spectral index of -0.81 ± 0.03. This would imply $\alpha_{\rm inj} \sim -0.3$ for a simple shock model. The flattest possible spectral index is -0.5 from DSA, suggesting that the relic recently brightened or just formed. In this case no equilibrium

has yet been reached between the electron cooling and injection within the observed frequency range below 1369 MHz. Another possibility is that the area over which we integrate the flux does not include all of the relic emission. It could be that some of this steep-spectrum emission is blended with that of the radio halo. Finally, the flat radio spectrum could also imply that DSA is not fully understood or that the radio emitting electrons do not originate from the DSA mechanism. If the relic traces a recently formed shock, then spectral steepening is expected at high-frequencies. Clarke & Ensslin (2006) indeed reported a steeper spectral index of −1.2 between 1369 and 1703 MHz for the relic.

For a typical magnetic field strength of 2 μG for the relic (Clarke & Ensslin 2006) and $\nu_{\rm brk}$ = 1400 MHz, the spectral age is about 0.05 Gyr. Berrington et al. (2002) proposed that A2256 is undergoing a triple merger event. One between a subcluster and the primary cluster and one between the primary cluster and subcluster (or the primary cluster only) with a smaller galaxy group. The relative velocity between the subcluster and primary cluster is estimated to be $\sim$ 2000 km s^{-1} and they are near the time of the first close passage of the subcluster and primary cluster centers. The group is infalling from the north. The "primary cluster–subcluster" merger has a mass ratio of about 3 and the "primary cluster (+subcluster)–group" merger event has a mass ratio of about 10. Miller et al. (2003) argued that the "primary cluster–galaxy group" merger is responsible for the radio relic and that the merger event is viewed 0.3 Gyr after the core passage. From the radio spectra alone it is not possible to disentangle the merger scenario, but usually the strongest shocks form after core passage and the flat integrated radio spectrum implies that the relic only recently formed, $\lesssim$ 0.1 Gyr or so. The relic in A2256 is thus probably seen at a relatively early stage, just after core passage, compared to some of the double radio relic clusters (e.g., Röttgering et al. 1997; Bagchi et al. 2006; Bonafede et al. 2009b; van Weeren et al. 2011c). Further flux measurements above 2 GHz are needed to better constrain the high-frequency end of the spectrum and confirm the radio spectrum steepens here.

No shock has been found so far in X-ray observations. Although, given the large extent of the relic in both the NS and EW directions we are probably not viewing the relic close to edge-on, making it more difficult to detect a shock. For an edge-on shock/relic one would expect a much larger ratio between the largest physical extent and the relic width (e.g., van Weeren et al. 2010). Because of the large size of the relic it is unlikely we are seeing fossil radio plasma compressed by a shock wave since radiative energy losses during the time it takes to compress a several hundred kiloparsec sized radio ghost would remove most of the electrons responsible for the observable radio emission Clarke & Ensslin (2006). In addition, we would expect steep curved radio spectra due to synchrotron and IC losses.

The spectral index of the radio halo was measured by summing the flux in the region around source D, see Fig. 12.4 (right panel). In this region the halo is detected at the 1–3σ level per beam in the LOFAR 63 MHz image. The flux was measured from the 63 MHz image used for the spectral index map. We sumed the flux over the same region in the 351 MHz WSRT and 1369 MHz VLA D-array (Clarke & Ensslin 2006) images. The resulting radio spectrum is shown in Fig. 12.8. The 63–351 MHz spectral index is -1.3 ± 0.1 and the 351–1369 MHz spectral index is -1.1 ± 0.1. In the image made with robust 0.5 weighting (Fig. 12.4) we measure a halo flux that is a factor of 1.5 higher than in the uniform weighted tapered image from the spectral index map (summing the flux over the same region). With this higher flux the 63–351 MHz spectral index would be about −1.5. Therefore the low-frequency spectral index is probably steeper than the high-frequency one. This low-frequency steepening was also reported by Kale & Dwarakanath (2010) and is consistent with a combination of spectra from (at least)

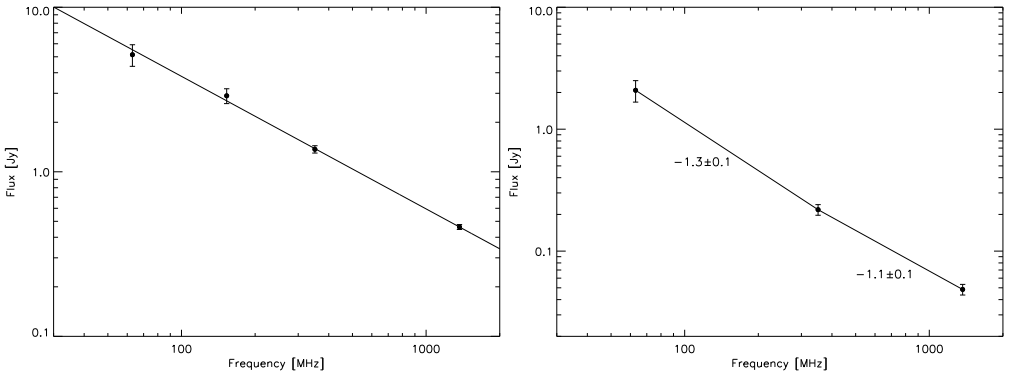

Figure 12.8: Left: Radio spectrum of the relic. Flux measurements from Clarke & Ensslin (2006), Brentjens (2008), and Intema (2009) were included. Solid line is a power-law fit to the flux measurements. Right: Radio halo spectrum from flux measurements summed over the region indicated in Fig. 12.4.

two populations of relativistic electrons.

Three different possibilities to explain this would be: (1) a model where protons and their secondaries live in a turbulent medium and get re-accelerated. The re-acceleration time scale here is very long (about 1 Gyr), meaning that most of the signal at higher frequencies is dominated by the process of injection of secondaries (with a flatter spectrum), while at lower frequencies turbulent re-acceleration boosts the radio emission (Brunetti & Lazarian 2011), (2) a model where there is a halo with a steep turbulent re-acceleration spectrum, while some projected emission from the relic (in the northern part) is superimposed on the halo emission. In this case the 1369 MHz flux is dominated by the tail of the relic emission downstream that is projected onto the halo, or (3) an "inhomogeneous" turbulent re-acceleration model, in this case the turbulence is not homogeneous over the emitting volume which leads to a distribution of different spectral components.

With only three data points it is not possible to distinguish between these models, but with future (LOFAR) observations it will be possible to much better determine the low-frequency spectrum. This opens new theoretical questions and it would be interesting to determine if low-frequency spectral steepening is unique to Abell 2256 or whether it also occurs for other radio halos.

12.4 Conclusions

We have presented LOFAR LBA observations between 67 and 18 MHz of the cluster Abell 2256. We focussed mainly on the 63 MHz map as at lower frequencies ionospheric phase distortions were severe. At 63 MHz we detect both the radio halo and main radio relic. The integrated spectral index we find for the relic is consistent with being a power-law with $\alpha = -0.81 \pm 0.03$. The integrated radio spectrum of the relic is quite flat, which could mean that the relic has only recently been formed, within the last ~ 0.1 Gyr. For the radio halo there are indications of a low-frequency spectral steepening, this was previously also reported by Kale & Dwarakanath (2010).

Additional flux measurements are needed to better determine the low-frequency spectrum of the halo and the origin of the convex spectrum.

We detected a recently found steep spectrum source to the west of the cluster center, located roughly at the end of the head-tail source C. For this source we find an extremely steep spectral index of -2.3 ± 0.4 between 63 and 153 MHz. This steep spectrum source could be an older part of the tail of source C. For source F2 we find the spectral index flattens to -0.95 between 63 and 153 MHz. The origin of the source remains unclear.

In the future we plan to extend our investigation to lower frequencies. For this, ionospheric calibration schemes will be important to retain enough spatial resolution to separate the contribution from the various complex sources in the cluster.

Acknowledgements. LOFAR, the Low Frequency Array designed and constructed by ASTRON, has facilities in several countries, that are owned by various parties (each with their own funding sources), and that are collectively operated by the International LOFAR Telescope (ILT) foundation under a joint scientific policy. We thank Michiel Brentjens and Ming Sun for providing the 351 MHz WSRT and Chandra X-ray image, respectively. RJvW acknowledges funding from the Royal Netherlands Academy of Arts and Sciences.